Journal of
Synchrotron
Radiation

ISSN 1600-5775

Received 24 September 2013
Accepted 16 February 2014

Three-dimensional coherent diffractive imaging on non-periodic specimens at the ESRF beamline ID10

Y. Chushkin,[a]* F. Zontone,[a] E. Lima,[b] L. De Caro,[c] P. Guardia,[d] L. Manna[d] and C. Giannini[c]

[a]European Synchrotron Radiation Facility, BP 220, F-38043 Grenoble, France, [b]Photon Sciences Directorate, Brookhaven National Laboratory, Upton, NY 11973-5000, USA, [c]Istituto di Cristallografia, via Amendola 122/O, 70126 Bari, Italy, and [d]Istituto Italiano di Tecnologia, via Morego 30, 16163 Genova, Italy. *E-mail: chushkin@esrf.fr

The progress of tomographic coherent diffractive imaging with hard X-rays at the ID10 beamline of the European Synchrotron Radiation Facility is presented. The performance of the instrument is demonstrated by imaging a cluster of Fe_2P magnetic nanorods at 59 nm 3D resolution by phasing a diffraction volume measured at 8 keV photon energy. The result obtained shows progress in three-dimensional imaging of non-crystalline samples in air with hard X-rays.

Keywords: coherent diffraction imaging; phase-retrieval; randomly assembled nanostructures.

1. Introduction

Modern third-generation synchrotron radiation sources produce intense spatially coherent X-ray beams several orders of magnitude higher than previously available. This has opened possibilities for development of new X-ray scattering techniques such as coherent diffraction imaging (CDI) (Chapman & Nugent, 2010). CDI is a lensless imaging method in which a coherent X-ray beam, transmitted through or reflected by an isolated object, freely propagates to a two-dimensional (2D) detector where its far-field diffraction pattern is registered (Chapman & Nugent, 2010). The idea of image reconstruction from coherent diffraction can be traced back to the work of Sayre (Sayre, 1952) in 1952, who discussed the effect of a finer-than-crystallographic sampling of a diffraction pattern. The missing phase can be recovered from the measured Fourier amplitude by phase-retrieval algorithms (Fienup, 1982; Elser, 2003) when the speckle pattern in one, two and three dimensions is oversampled by at least a factor of 2, $2^{1/2}$ and $2^{1/3}$ in each dimension, respectively (Miao *et al.*, 1998). The first experimental proof for X-rays dates back to 1999 (Miao *et al.*, 1999).

CDI has the potential of imaging objects with a spatial resolution limited by the wavelength of the probe. In practice, the resolution is restricted by the maximum scattering vector where the intensity is still reliably detected, and for biological specimens it is ultimately limited by radiation-induced damage (Howells *et al.*, 2009). CDI can provide images with higher resolution than that offered by physical optics (Chao *et al.*, 2005; Mimura *et al.*, 2010). So far the highest achieved resolution in CDI is around 11 nm in 2D (Nelson *et al.*, 2010) and 11–15 nm (Chapman *et al.*, 2006; Barty *et al.*, 2008) in 3D with soft X-rays, and 2 nm (Takahashi *et al.*, 2010) in 2D and 17–60 nm (Miao *et al.*, 2006, 2002; Jiang *et al.*, 2010) in 3D with hard X-rays. The main motivation to use hard X-rays stems from its high penetrating power. The absorption becomes negligible and the validity of the Born approximation can be extended for thicker objects or specimens with higher electron density. The structural complexity of thick objects (<10 µm) can only be revealed in 3D. Moreover, utilization of hard X-rays for CDI does not require a vacuum environment, facilitating sample manipulation, which is well suited for imaging biological samples with cryo-protection requiring a cold gas stream (Lima *et al.*, 2009).

The coherent hard X-rays are also successfully used in Bragg geometry for characterization of strain distribution in nanocrystalline materials (Robinson & Harder, 2009). Nanocrystals are inorganic particles made of a few hundred up to a few thousand atoms. They are available as semiconductors, oxides, metals and magnetic alloys and can be used for the design of complex architectures constructed by self-assembly (Murray *et al.*, 2000; Rogach *et al.*, 2002). This so-called 'bottom up' approach is a key concept in fundamental research used to organize individual units into nanoscale materials that could have novel chemical and physical properties in comparison with those of individual atoms or bulk. The main focus of research concerning the assembly of colloidal nanocrystals, considered as building blocks, has so far been directed toward their organization in ordered (or with a high degree of order) superstructures, either promoted by self-assembly processes or by means of external perturbations deliberately driving nanoparticle organization (Rogach, 2004; Shevchenko *et al.*, 2006, 2005; Carbone *et al.*, 2007; Baranov *et al.*, 2010; Miszta *et al.*, 2011). An alternative to periodically ordered self-assembled structures can be recognized in the end-to-end assembly of nanocrystals of controlled shapes

(Figuerola *et al.*, 2009). The vast variety of possible self-assembled structures requires a thorough investigation.

The structural characterization of the self-assembled nanoparticles is important for understanding both their collective properties and the self-assembly mechanism. X-ray scattering techniques, such as X-ray diffraction (XRD), small-angle X-ray scattering (SAXS), grazing-incidence XRD and grazing-incidence SAXS, are frequently used to study self-assembled periodic and more complex structures (Renaud *et al.*, 2009). They provide ensemble average structural information from the scattering volume and very often require modeling and simulations for the interpretation of the measured spectra. On the other hand, X-ray imaging such as transmission X-ray microscopy (Chao *et al.*, 2005) or CDI (Chapman & Nugent, 2010) can provide a high-resolution real-space image of a sample to visualize the non-periodic microscopic structure.

A successful CDI can be, however, difficult to obtain due to limited coherent flux available, low signal-to-noise ratio in the measured diffraction pattern, and computational complexity of phasing such data. Special care has to be exercised to deliver a high-quality coherent beam on a sample and to measure the diffraction pattern that brings a successful phase retrieval. In this paper we present the technical details of hard X-ray CDI in forward-scattering geometry. While the previously reported works used CCD detectors, here we used a 2D pixel X-ray detector with high dynamic range that simplifies the data acquisition and subsequent post-processing. The instrument performance is demonstrated by imaging of a non-periodic assembly of Fe_2P nanorods in three dimensions in air. The image of the object was reconstructed directly from the 3D diffraction pattern assembled from the 2D data sets measured at different angular tilts of the sample as done in early works (Miao *et al.*, 2002; Chapman *et al.*, 2006; Barty *et al.*, 2008). Alternatively, the equally sloped tomographic reconstruction method is used (Miao *et al.*, 2006; Jiang *et al.*, 2010) but it was not applied here.

2. Experimental details

The CDI experiment was conducted on the beamline ID10C at the European Synchrotron Radiation Facility. The beamline was built for small-angle X-ray scattering of coherent beams and X-ray photon correlation spectroscopy (XPCS). Because CDI relies on a plane-wave illumination, it is more sensitive to the quality of the beam in terms of coherence preservation than XPCS and the instrument has to be optimized accordingly (Lima *et al.*, 2009). A sketch of the optical scheme used in the experiment is shown in Fig. 1. An 8 keV X-ray beam from an undulator source was focused by two Be compound refractive lenses of radius 200 µm in nearly 1:1 geometry at the sample position 60 m downstream from the source. The X-ray beam was monochomatized by a water-cooled pseudo-channel-cut Si(111) monochromator ($\Delta\lambda/\lambda = 1.4 \times 10^{-4}$) diffracting in vertical geometry and situated at 56.5 m from the source. The monochromator was made of a highly polished single Si crystal cut into two pieces that are mounted on an invar holder to mimic the behaviour of a real channel-cut monochromator. The beam after the monochromator was cleaned from the high-order reflections by using two Si mirrors reflecting at a grazing-incidence angle of 0.2°. The beam-defining roller-blade slits of 10 µm × 10 µm opening placed 500 mm from the sample ensured the coherent illumination of the object with an estimated flux of 3×10^9 photons s^{-1}. The diffraction from the beam-defining slits was cleaned by the second roller-blade guard slits and finally by the Si blade guard slits. The roller-blade slits and Si mirrors are kept under vacuum with 15 µm-thick mica exit window. The monochomator, mirrors and mica window are key optical elements that can degrade the coherence of the beam. To minimize the loss of coherence, these elements were positioned in correspondence to the cleanest areas by monitoring the spatial homogeneity of the unfocused beam on a fluorescent screen at the sample position with an on-axis microscope. Once the optimal positioning was found, the lenses were inserted into the beam. The sample was placed on a high-precision goniometer rotating in the horizontal plane equipped with the on-axis microscope for sample localization and alignment on the rotation axis. The sample stage, the on-axis microscope and the Si blade guard slits are kept in air. Such a set-up is favorable for imaging frozen-hydrated biological specimens under cryostream (Lima *et al.*, 2009). X-rays scattered off the sample propagate to the detector through a vacuum flightpath. The flightpath's entrance window is 500 nm-thick Si_3N_4

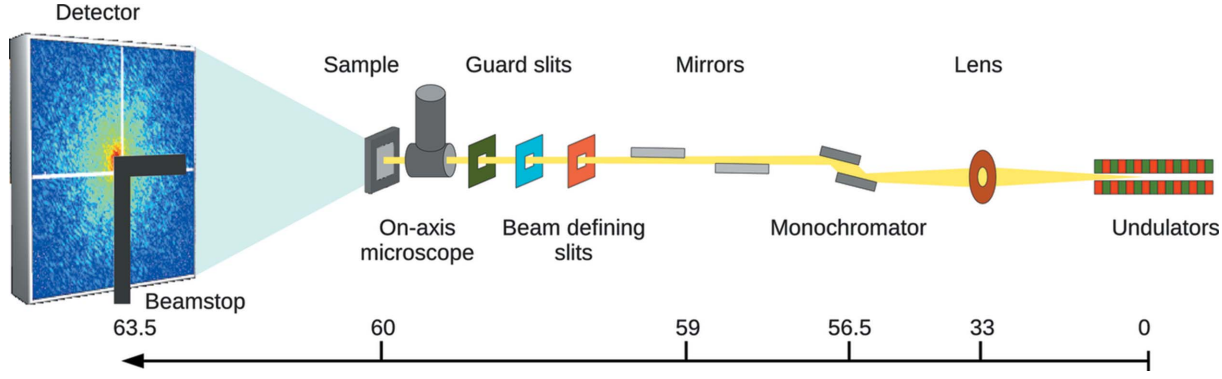

Figure 1
Sketch of the optical scheme used at the ID10 beamline (distances in meters).

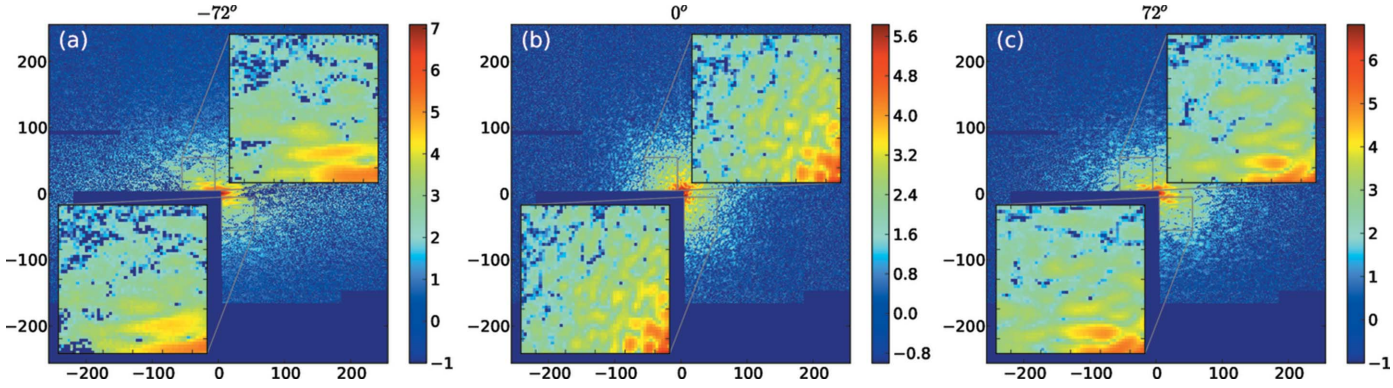

Figure 2
Diffraction patterns taken at −72, 0 and 72° sample tilts. The insets are zooms of the small part of the pattern. The bottom inset is rotated by 180° for comparison with the top inset. (*a*) The diffraction pattern shows small deviation from the centrosymmetry; (*b*,*c*) the diffraction patterns are centrosymmetric.

membrane and the exit window is 50 µm-thick Kapton film. An L-shape beamstop blocking the direct beam is mounted in vacuum at the end of the flightpath in front of a detector. The diffraction patterns were measured by a Maxipix 2 × 2 chip detector (Ponchut *et al.*, 2011) placed at 3.54 m from the sample. The detector has 516 × 516 pixels with 55 µm pixel size and zero readout noise. A high frame rate of 350 Hz and high counter depth (11180 counts) allow a high dynamic range of 2×10^5 counts s^{-1} $pixel^{-1}$ with 20% dead time. There is no need to take multiple exposures to increase the dynamic range as is done with CCD cameras. Instead, the measurement of a diffraction pattern is performed in an accumulation mode where individual 50 ms exposures are taken and added together by a device server to make one single image of the required exposure time.

To demonstrate the performance of the instrument we imaged a cluster made of magnetic Fe_2P nanorods deposited on a 100 nm-thick Si_3N_4 membrane (Fig. 3*a*). The Fe_2P nanorods (38 ± 12 nm/4 ± 1 nm, length/diameter) were synthesized by a slightly modified protocol from Park *et al.* (2004) and characterized by SQUID magnetometry (see supporting information[1]). The cluster was formed from a drop of the diluted colloidal suspension under spontaneous drying and self-assembly with a resultant random density variation. The diffraction patterns and the background were accumulated for 300 s each at two different detector positions to recover the intensities in the gaps between the chips. An inhomogeneous efficiency between individual pixels was corrected by the flat-field, and the pixels with high intensity were corrected for detector dead-time. The total duration of the measurements for 73 2D diffraction patterns taken for the sample tilts between −72° and +72° with a step of 2° lasted 24 h. The diffraction patterns for the sample tilts between −64° and +72° are centrosymmetric as shown in Figs. 2(*b*) and 2(*c*). We used this property to fill the pixels with missing data behind the beamstop with its centrosymmetric counterparts. The other two quadrants were averaged centrosymmetrically to improve the signal-to-noise ratio. The diffraction patterns for the sample tilts between −72° and −66° show a slight deviation from the centrosymmetry (Fig. 2*a*) and no centrosymmetric treatment was applied. At these angles the object attains its highest optical thickness. The specimen starts departing from the criteria for the weak-object approximation (Nugent, 2010) which causes slight non-centrosymmetry of the diffraction patterns. Finally, the 3D speckle pattern was combined using nearest-neighbor interpolation. Because the linear oversampling ratio was ∼2.85, we did not use binning to increase the signal-to-noise ratio. The original data are reported in Fig. S1 of the supporting information, plotted every 12°.

3. Result and discussion

Self-assembly is widely used in the fabrication of nanoscaled 2D and 3D structures. Depending on experimental conditions one can obtain well ordered arrays of nanoparticles or clusters from a random particle distribution. The latter case applies to the cluster studied here. The disordered character of the sample, as shown by the scanning electron microscopy (SEM) image (Fig. 3*a*), its size and composition make it the ideal object for 3D imaging by hard X-rays.

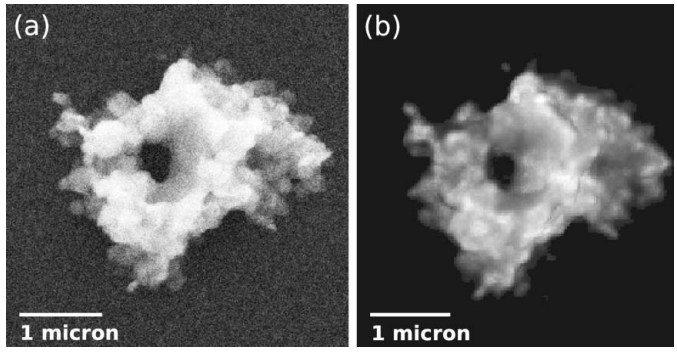

Figure 3
SEM of the Fe_2P cluster (*a*) and a 2D projection of the reconstructed image (*b*).

[1] Supporting information for this paper is available from the IUCr electronic archives (Reference: GB5019).

To retrieve a 3D image of the object we applied the hybrid input–output phase-retrieval algorithm (Fienup, 1982) to the 3D diffraction pattern consisting of 420 × 420 × 420 voxels. The 3D data set contains several regions with undefined intensities. The information in the central 12 × 12 × 12 voxels is missing due to the beamstop blocking the direct beam. The limited range of the sample tilts results in a missing wedge of 36°, beyond ±72°. Finally, a discrete angular sampling with 2° does not cover all voxels at large q values. The full coverage of voxels at the corners of the diffraction pattern requires a 0.2° angular increment. In the presented case 90% of the voxels in the diffraction volume are missing. Nevertheless, the available 10% of intensity is sufficient for the successful phase-retrieval process. The algorithm searches for the lost phase iterating between the Fourier and real spaces using a 3D fast Fourier transform (FFT). The convergence to the right solution is achieved by imposing known constraints. Starting from the initial guess, *i.e.* a 90 × 90 × 90 voxels cube of random density $\rho_j(x, y, z)$, we calculate the FFT to obtain the Fourier amplitude $A_j(q_x, q_y, q_z)$ and the phase $\varphi_j(q_x, q_y, q_z)$. The Fourier amplitude is replaced by the measured amplitude $[I(q_x, q_y, q_z)]^{1/2}$, and the new density $\rho_j'(x, y, z)$ is calculated by the inverse FFT of $[I(q_x, q_y, q_z)]^{1/2} \exp[i\varphi_j(x, y, z)]$. The density for the next iteration is generated by

$$\rho_{j+1}(x, y, z) = \begin{cases} \rho_j'(x, y, z), & (x, y, z) \in S, \\ \rho_j(x, y, z) - \beta\rho_j'(x, y, z), & (x, y, z) \notin S, \end{cases} \quad (1)$$

where β is the feedback parameter (here $\beta = 0.9$) and S is the object support. The object support represents points in real space that confine the object and is not known *a priori*. However, it was refined during the reconstruction process using the shrinkwrap method (Marchesini *et al.*, 2003). The convergence of the algorithm was monitored by the error function

$$E = \frac{\sum \left| A_j(q_x, q_y, q_z) - [I(q_x, q_y, q_z)]^{1/2} \right|^2}{\sum I(q_x, q_y, q_z)}. \quad (2)$$

The image reconstruction was obtained after 1500 iterations. The final image is the result of averaging 33 aligned reconstructions with the smallest error E obtained from random starting densities. To align the images, the image offsets were estimated using 3D FFT and then corrected accordingly with a pixel precision. The 2D projection of the resulting image is shown in Fig. 3(*b*). It is in very good agreement with the SEM in Fig. 3(*a*), which allows us to check the fidelity of the reconstruction process. The reconstructed 3D image of the cluster is shown in Figs. 4 and 5 and in Fig. S2 of the supporting information.

The principal attractiveness of the CDI technique is the ability of high-resolution imaging. In practice, the actual resolution is limited by the detector active area, the quality of the diffraction patterns and finally the beam damage of the sample. For a known object the resolution of the reconstructed image is determined from the line scan through a sharp feature. Because the fine structure of our object is not known *a priori*, the quality of the reconstruction is quantified using

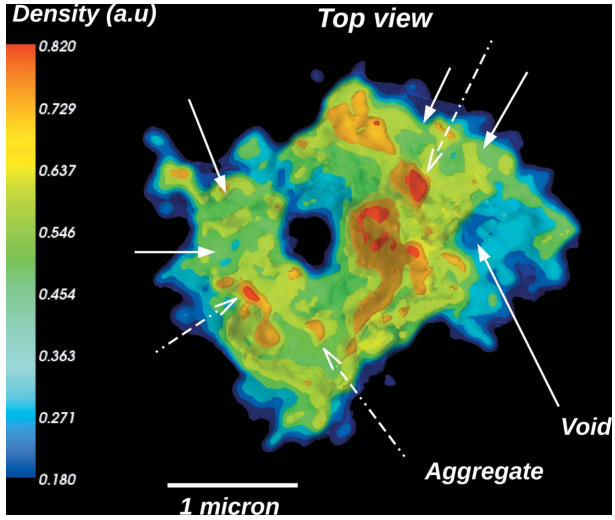

Figure 4
Top view of the cluster using 3D semi-transparent iso-surface rendering. Continuous arrows show several voids; dashed arrows point to the high-density aggregates.

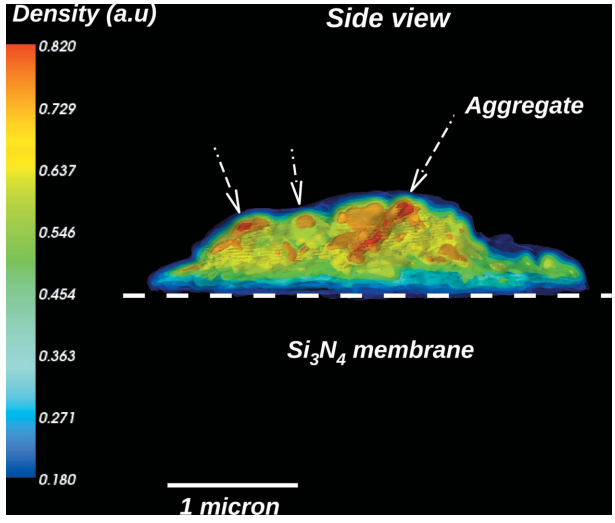

Figure 5
Side view of the cluster using 3D semi-transparent iso-surface rendering. Dashed arrows point to the high-density aggregates.

the phase-retrieval transfer function (PRTF) (Chapman *et al.*, 2006),

$$\mathrm{PRTF}(f) = \sum_{f=\mathrm{const}} A(f) \Big/ \sum_{f=\mathrm{const}} [I(f)]^{1/2}. \quad (3)$$

The PRTF is the ratio of the Fourier amplitude of the reconstructed image $A(f)$ to the measured $[I(f)]^{1/2}$ as a function of the spatial frequency f or equivalently of the half-period resolution. We used a conservative estimate of the resolution given by PRTF = 0.5. The function is shown in Fig. 6. In the experimental configuration used, the maximum theoretical resolution that could be achieved is 24 nm, the real-space voxel size. However, the estimated half-period resolution of the reconstructed image is around 59 nm. There could be many factors that degrade the resolution. The Maxipix is considered as a noise-free detector; the signal-to-noise ratio

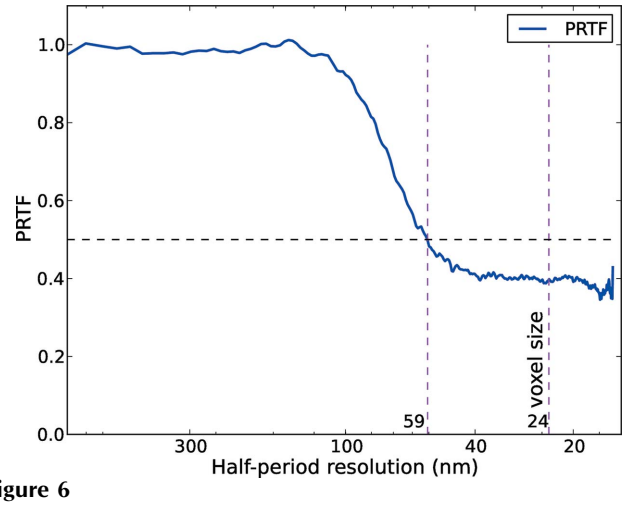

Figure 6
PRTF of the reconstructed image (blue line). The horizontal line corresponds to PRTF = 0.5. The vertical line at 59 nm corresponds to cut-off frequencies at 0.5 PRTF and that at 24 nm indicates the real-space voxel size.

(SNR) of the measured data is largely determined by the shot noise. If we use a threshold of SNR = 3, as adopted by crystallographers (Acharya & Lloyd, 2005), then we can expect a resolution of 59 nm. In addition, the large angular increment used does not allow the full 3D data sampling at high spatial frequencies. Indeed the 0.2° angular increment is required for a full data sampling instead of the 2° used. Moreover, the missing wedge, due to the restricted sample tilts, degrades resolution along the beam propagation direction (Chapman *et al.*, 2006). Recently, a technique that takes into account the noise during the phase-retrieval procedure (Martin *et al.*, 2012) was demonstrated for experimental diffraction data with high linear oversampling ratio (>8). However, when the linear oversampling ratio is small (<6), the method is not efficient (Martin, 2012) and we could not apply it to our data. Achieving 10–20 nm resolution should be possible by using a more intense incident beam, finer angular increments, and a detector with a larger number of pixels.

The image resolution is not sufficient to resolve the individual nanorods but we can easily identify the dense aggregates and voids in Fig. 4 as indicated by dashed and continuous arrows, respectively. We remark that the density in the cluster is distributed randomly and not at the bottom of the cluster, as one would expect for sedimentation. It can be assumed that some of the dense aggregates existed in the original dilute suspension but others were formed during the solvent evaporation. Also the paramagnetic nature of the nanorods at room temperature (see magnetic characterization reported in the supporting information) cannot play an important role in self-assembly. The formation of voids and high-density areas on the top and in the middle of the cluster is driven by complex fluid hydrodynamics in the evaporating sessile drop.

4. Summary and conclusions

In this work we have presented details of the instrumentation for conducting hard X-ray tomographic CDI on non-crystalline microscopic objects. The performance of the set-up has been demonstrated by imaging a Fe_2P nanorods assembly at 59 nm 3D resolution. The image reconstruction has been obtained using an iterative phase-retrieval algorithm applied to the sample's 3D diffraction pattern that was assembled from 73 measured 2D diffraction data. The reconstructed electron density distribution of the Fe_2P cluster in three dimensions points to the complex hydrodynamic effects governing the cluster formation. To improve resolution down to the sub-20 nm range an increase in coherent X-ray flux and a detector with at least 1200 × 1200 pixels are needed. Utilization of hard X-rays for CDI does not require a vacuum environment, facilitating sample manipulation, which is well suited for imaging biological samples with cryo-protection requiring a cold gas stream (Lima *et al.*, 2009). The high-resolution 3D imaging of biological and buried objects is expected to become a well established technique in the near future.

The authors would like to acknowledge Irina Snigireva for SEM characterization, Cyril Ponchut for help with the Maxipix detector, Michael Reynolds for a careful proof-reading of the manuscript, and the ID10 beamline staff for the technical support. Jianwei Miao is acknowledged for fruitful discussions.

References

Acharya, K. R. & Lloyd, M. D. (2005). *Trends Pharmacol. Sci.* **26**, 10–14.
Baranov, D., Fiore, A., van Huis, M., Giannini, C., Falqui, A., Lafont, U., Zandbergen, H., Zanella, M., Cingolani, R. & Manna, L. (2010). *Nano Lett.* **10**, 743–749.
Barty, A., Marchesini, S., Chapman, H. N., Cui, C., Howells, M. R., Shapiro, D. A., Minor, A. M., Spence, J. C., Weierstall, U., Ilavsky, J., Noy, A., Hau-Riege, S. P., Artyukhin, A. B., Baumann, T., Willey, T., Stolken, J., van Buuren, T. & Kinney, J. H. (2008). *Phys. Rev. Lett.* **101**, 055501.
Carbone, L., Nobile, C., De Giorgi, M., Sala, F. D., Morello, G., Pompa, P., Hytch, M., Snoeck, E., Fiore, A., Franchini, I. R., Nadasan, M., Silvestre, A. F., Chiodo, L., Kudera, S., Cingolani, R., Krahne, R. & Manna, L. (2007). *Nano Lett.* **7**, 2942–2950.
Chao, W., Harteneck, B. D., Liddle, J. A., Anderson, E. H. & Attwood, D. T. (2005). *Nature (London)*, **435**, 1210–1213.
Chapman, H. N., Barty, A., Noy, A., Hau-Riege, S. P., Cui, C., Howells, M. R., Rosen, R., He, H., Spence, J. C. H., Weierstall, U., Beetz, T., Jacobsen, C. & Shapiro, D. (2006). *J. Opt. Soc. Am. A*, **23**, 1179–1200.
Chapman, H. N. & Nugent, K. A. (2010). *Nat. Photon.* **4**, 833–839.
Elser, V. (2003). *J. Opt. Soc. Am. A*, **20**, 40–55.
Fienup, J. R. (1982). *Appl. Opt.* **21**, 2758–2769.
Figuerola, A., Franchini, I. R., Fiore, A., Mastria, R., Falqui, A., Bertoni, G., Bals, S., Van Tendeloo, G., Kudera, S., Cingolani, R. & Manna, L. (2009). *Adv. Mater.* **21**, 550–554.
Howells, M. R., Beetz, T., Chapman, H. N., Cui, C., Holton, J. M., Jacobsen, C. J., Kirz, J., Lima, E., Marchesini, S., Miao, H., Sayre, D., Shapiro, D. A., Spence, J. C. H. & Starodub, D. (2009). *J. Electron Spectrosc. Relat. Phenom.* **170**, 4–12.
Jiang, H., Song, C., Chen, C.-C., Xu, R., Raines, K. S., Fahimian, B. P., Lu, C.-H., Lee, T.-K., Nahashima, A., Urano, J., Ishikawa, T., Tamanoi, F. & Miao, J. (2010). *Proc. Natl Acad. Sci.* **107**, 11234–11239.

Lima, E., Wiegart, L., Pernot, P., Howells, M., Timmins, J., Zontone, F. & Madsen, A. (2009). *Phys. Rev. Lett.* **103**, 198102.
Marchesini, S., He, H., Chapman, H. N., Hau-Reige, S. P., Noy, A., Howells, M. R., Weierstall, U. & Spence, J. C. H. (2003). *Phys. Rev. B*, **68**, 140101R.
Martin, A. V. (2012). Private communication.
Martin, A. V. *et al.* (2012). *Opt. Express*, **20**, 16650–16661.
Miao, J., Charalambous, P., Kirz, J. & Sayre, D. (1999). *Nature (London)*, **400**, 342–344.
Miao, J., Chen, C. C., Song, C., Nishino, Y., Kohmura, Y., Ishikawa, T., Ramunno-Johnson, D., Lee, T. K. & Risbud, S. H. (2006). *Phys. Rev. Lett.* **97**, 215503.
Miao, J., Ishikawa, T., Johnson, B., Anderson, E. H., Lai, B. & Hodgson, K. O. (2002). *Phys. Rev. Lett.* **89**, 088303.
Miao, J., Sayre, D. & Chapman, H. N. (1998). *J. Opt. Soc. Am. A*, **15**, 1662–1669.
Mimura, H., Handa, S. & Kimura, T. (2010). *Nat. Phys.* **6**, 122–125.
Miszta, K., de Graaf, J., Bertoni, G., Dorfs, D., Brescia, R., Marras, S., Ceseracciu, L., Cingolani, R., van Roij, R., Dijkstra, M. & Manna, L. (2011). *Nat. Mater.* **10**, 872–876.
Murray, C. B., Kagan, C. R. & Bawendi, M. G. (2000). *Annu. Rev. Mater. Sci.* **30**, 545–610.
Nelson, J., Huang, X., Steinbrener, J., Shapiro, D., Marchesini, S., Neiman, A. M., Turner, J. J. & Jacobsen, C. (2010). *Proc. Natl Acad. Sci.* **107**, 7235–7239.
Nugent, K. A. (2010). *Adv. Phys.* **59**, 1–99.
Park, J., Koo, B., Hwang, Y., Bae, C., An, K., Park, J. G., Park, H. M. & Hyeon, T. (2004). *Angew. Chem. Int. Ed.* **43**, 2282–2285.
Ponchut, C., Rigal, J. M., Clément, J., Papillon, E., Homs, A. & Petitdemange, S. (2011). *J. Instrum.* **6**, C01069.
Renaud, G., Lazzari, R. & Leroy, F. (2009). *Surf. Sci. Rep.* **64**, 255–380.
Robinson, I. & Harder, R. (2009). *Nat. Mater.* **8**, 291–298.
Rogach, A. L. (2004). *Angew. Chem.* **116**, 150–151. [also (2004). *Angew. Chem. Int. Ed.* **43**, 148–149.]
Rogach, A. L., Talapin, D. V., Shevchenko, E. V., Kornowski, A., Haase, M. & Weller, H. (2002). *Adv. Funct. Mater.* **12**, 653–664.
Sayre, D. (1952). *Acta Cryst.* **5**, 843.
Shevchenko, E. V., Talapin, D. V., Kotov, N. A., O'Brien, S. & Murray, C. B. (2006). *Nature (London)*, **439**, 55–59.
Shevchenko, E. V., Talapin, D. V., O'Brien, S. & Murray, C. B. (2005). *J. Am. Chem. Soc.* **127**, 8741–8747.
Takahashi, Y., Nishino, Y., Tsutsumi, R., Zattsu, N., Matsubara, E., Yamauchi, K. & Ishikawa, T. (2010). *Phys. Rev. B*, **82**, 214102.